



An electroactive hybrid biointerface for enhancing neuronal differentiation and axonal outgrowth on bio-subretinal chip



Jia-Wei Yang^{a,b,1}, Chong-You Chen^{a,b,1}, Zih-Yu Yu^a, Johnson H.Y. Chung^c, Xiao Liu^c, Chung-Yu Wu^d, Guan-Yu Chen^{a,b,*}

^a Institute of Biomedical Engineering, College of Electrical and Computer Engineering, National Yang Ming Chiao Tung University, Hsinchu, 300093, Taiwan

^b Department of Electronics and Electrical Engineering, College of Electrical and Computer Engineering, National Yang Ming Chiao Tung University, Hsinchu, 300093, Taiwan

^c ARC Centre of Excellence for Electromaterials Science, Intelligent Polymer Research Institute, University of Wollongong, Wollongong, NSW 2500, Australia

^d Institute of Electronics, National Yang Ming Chiao Tung University, Hsinchu, 300093, Taiwan

ARTICLE INFO

Keywords:

Graphene oxide
Biointerface
Neuronal cell
Retinal chip
Micropattern

ABSTRACT

Retinal prostheses offer viable vision restoration therapy for patients with blindness. However, a critical requirement for maintaining the stable performance of electrical stimulation and signal transmission is the biocompatibility of the electrode interface. Here, we demonstrated a functionalized electrode–neuron biointerface composed of an annealed graphene oxide–collagen (aGO–COL) composite and neuronal cells. The aGO–COL exhibited an electroactive 3D crumpled surface structure and enhanced the differentiation efficiency of PC-12 cells. It is integrated into a photovoltaic self-powered retinal chip to develop a biohybrid retinal implant that facilitates biocompatibility and tissue regeneration. Moreover, aGO–COL micropatterns fabricated via 3D bioprinting can be used to create neuronal cell microarrays, which supports the possibility of retaining the high spatial resolution achieved through electrical stimulation of the retinal chip. This study paves the way for the next generation of biohybrid retinal implants based on biointerfaces.

1. Introduction

The leading cause of age-related macular degeneration and retinitis pigmentosa is partial or complete necrosis of the photoreceptor in the retina, which can cause blurred vision and even blindness [1,2]. Only surgery or medications can be used to delay disease progression. Recently, emerging retinal prostheses have demonstrated the potential to restore functional vision in patients [3–5]. Retinal prostheses can substitute artificial electrical components for the light-responsive function of photoreceptor cells in the retina, converting incoming light into electrical impulses, and transmitting them to residual retinal nerve cells for imaging [6,7]. Nonetheless, there are still some challenges concerning biocompatibility between electrode interfaces of implantable prostheses and residual tissue, especially low interaction and transplant rejection [8,9]. An urgent demand for improving this issue has urged scientists to develop biohybrid retinal prostheses [10], which integrate electroactive retinal nerve cells with synthetic electrodes to enhance bioelectrode

interface compatibility while providing unique opportunities for tissue regeneration. In addition, biohybrid retinal prostheses and residual retinal cells within the body can interconnect through axons of neurons to improve the electrical pulse transmission efficiency [11,12]. However, conventional metal electrodes exhibit low charge injection and capacitance, resulting in abnormal electrochemical reactions during electrical stimulation and transmission [13–15]. In this case, many cellular molecules and free ions are deposited on the electrode surface, affecting the viability of nerve cells and damaging the electrodes. Moreover, the mechanical properties of metal electrodes are generally unsuitable for cell attachment and connection, which reduces the electrical activation efficiency [16,17].

It is worth mentioning that nanomaterial-modified electrodes can effectively address the limitations of their mechanical and biological properties [18,19]. One of the most widely used nanomaterials is graphene oxide (GO), a derivative of graphene, which has excellent physicochemical and functional properties [20,21]. In addition, the edges and

* Corresponding author. Institute of Biomedical Engineering, College of Electrical and Computer Engineering, National Yang Ming Chiao Tung University, Hsinchu, 300093, Taiwan.

E-mail address: guanyu@nycu.edu.tw (G.-Y. Chen).

¹ The authors contributed equally to this work.

<https://doi.org/10.1016/j.mtbio.2022.100253>

Received 10 January 2022; Received in revised form 14 March 2022; Accepted 31 March 2022

Available online 5 April 2022

2590-0064/© 2022 Published by Elsevier Ltd. This is an open access article under the CC BY-NC-ND license (<http://creativecommons.org/licenses/by-nc-nd/4.0/>).

basal planes of GO have abundant oxygen-containing functional groups (e.g., hydroxyl and carboxyl groups) as reaction sites for chemical and physical modifications, which provide advantages for manipulating surface properties for specialized biomedical applications [22,23]. As an example, we previously demonstrated that GO-coated substrates enable pre-concentration of nutrients and grafting of peptides on the substrate surface to enhance the osteogenic differentiation efficiency of human mesenchymal stem cells [24]. More importantly, we have recently attempted to use printed GO micropatterns as a biointerface for the electrode surfaces of retinal prosthesis chips [25]. Compared with the bare electrodes of the retinal chip, the GO micropatterned electrodes significantly improved the growth and attachment of retinal pigment epithelial cells on the electrode surface, which supports the potential of GO as an electrode interface for biohybrid retinal prostheses [26].

To expand the applicability of GO to biohybrid electronic devices, the optimization of its conductivity must be considered. One direct approach to improving the GO conductivity is to reduce the oxygen content through high-temperature or chemical processes to obtain reduced GO (rGO) [27,28]. These rGO lack excellent functionalization properties because they lose a significant amount of oxygen functional groups [29]. Another practical approach is to control the surface topology of GO [30].

For example, the formation of crumpled or wrinkled GO structures can effectively improve the physicochemical properties [31–33]. However, such crumpled three-dimensional (3D) GO materials require complex non-conventional fabrication techniques which are not widely used. Earlier, we have successfully developed a unique mild thermal annealing procedure to modify GO so that the same planar structure can provide superior physical and chemical properties of both GO and graphene [34]. The annealed graphene oxide (aGO) not only increases the number of the sp^2 domain to increase the conductivity but also considerably maintains the oxygen functional groups, thereby exhibiting the advantages of functional surface modification for biomedical applications [24,35,36]. With this unique feature, aGO has an extraordinary ability to develop multifunctional structural biocomposites and provides enormous advantages for implantable bioelectronic devices. Therefore, as an innovative biomaterial concept for biohybrid retinal prostheses, aGO can incorporate extracellular matrix (ECM) and/or small molecules to produce functional composites with high compatibility and electrical conductivity [37,38].

Here, we present a concept of using aGO-based composite coupling neural cells as a biointerface for the next generation of biohybrid retinal prostheses (Fig. 1). The aGO-COL composite is produced by crosslinking

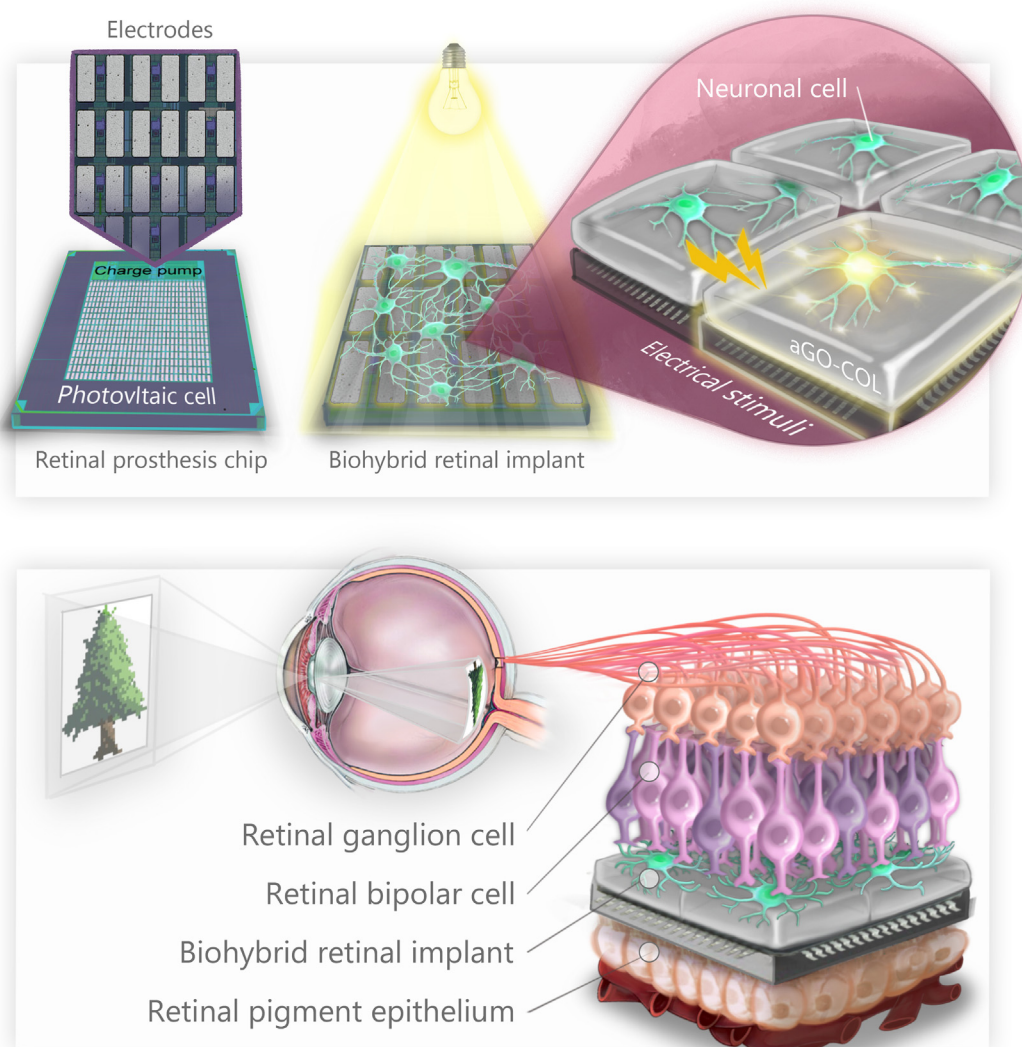


Fig. 1. The electroactive aGO-COL biointerface enhance the differentiation and growth of neuronal cells and subsequently integrate with the photovoltaic-powered retinal chip to develop a biohybrid retinal implant. The aGO-COL micropattern was accurately generated by a 3D bioprinter to support the creation of neuronal cell microarrays, which allows response to high spatial resolution of electrical stimulation of the retinal chip. Therefore, such a biohybrid retinal implant has the potential to provide great advantages that not only improves the biocompatibility of the neuron-electrode interface but also realizes tissue regeneration therapy.

reaction of aGO and collagen (COL) with a 3D crumpled structure. PC-12 cells, a typical neuron-like cell, are used instead of a limited source of retinal ganglion cells (RGCs) to assess neural differentiation on subretinal electrodes. Compared with the original GO, the aGO increases the conductivity of the electrodes by over 59%. Meanwhile, the aGO-COL-coated substrate with a crumpled structure can effectively improve the neurite differentiation and growth of PC-12 cells and increase the efficiency of electrical stimulation from light to electrical pulse signals in implantable retinal prostheses. Moreover, aGO-COL can be used with micropattern printing to create live cell arrays. This novel hybrid biomaterial demonstrates advantages that are not commonly available at interfaces using the GO or ECM alone, providing an unprecedented capability for cell-electrode interface application on retinal prostheses and implantable bioelectronic devices.

2. Material and methods

2.1. Preparation of the aGO and aGO-COL composite

A 4 mg/mL GO aqueous solution (Sigma-Aldrich, 777676) was first diluted with deionized water to 300 µg/mL and placed in an oven at 80 °C for 3, 5, and 9 days. The solution was then dispersed using an ultrasonic probe sonicator and filtered using a 1.2 µm syringe filter to obtain the aGO solution. For the synthesis of aGO-COL composites, carboxyl groups of the aGO solution were activated through the EDC/NHS coupling reaction for 1 h; it was then mixed with type I collagen from rat tails (Thermo Fisher Scientific, A1048301) for 1 h. Three different aGO weight percentages in aGO-COL were used in the experiments: 16%, 32%, and 64% (w/w, aGO/COL).

2.2. Characterization of the aGO and aGO-COL composite

The sheet resistivity of the aGO was measured using a four-point probe sheet resistivity measurement system (KeithLink Technology, LRS4-TG) in four-wire mode. The automatically measured parameters were a voltage of 2.1 V, a current of 100 nA, and an accurate resistance value range of 2–200 MΩ.

The chemical compositions of the GO, aGO, and aGO-COL samples were analyzed by X-ray photoelectron spectroscopy (XPS, Thermo Fisher Scientific, ESCALAB Xi⁺) and Fourier-transform infrared spectroscopy (FTIR, Bruker, Vertex 80v). All XPS spectra were calibrated with the C1s peak binding energy (284.6 eV for neutral carbon (C(sp²))), and the peak identification was performed using XPSPEAK41 software with a standard XPS database as a reference. In the C1s orbital, the fitted peaks correspond to specific carbon species with different chemical valences, namely C–C/C=C (284.6 eV), C–O/C–OH (285.7 eV), and C=O/C–NH (288.2 eV). In the N1s orbital, the fitted peaks correspond to N–C (399.2 eV), N=C (400.2 eV), and N–C=O (401.7 eV). In the FTIR spectra, the peaks observed corresponded to C–H (2700 cm⁻¹), C–OH (3343 cm⁻¹), C=O (1650 cm⁻¹), N–H (1560–1640 cm⁻¹ and 3400–3500 cm⁻¹), and C–N (1100–1300 cm⁻¹).

The microstructure of the aGO-COL was determined using a scanning electron microscope (SEM, Hitachi, SU-8010). The samples were first plated with platinum for 60 s and then detected with a 15-kV electron beam at a magnification of 15 kX. The topography information of the aGO-COL was acquired using atomic force microscopy (AFM, Bruker, Dimension Edge AFM). The samples were scanned in a frequency of 0–300 Hz and a voltage of 0.5 V in a range of 1 µm × 1 µm under tapping mode operation.

2.3. Electrochemical analysis of the aGO-COL composite

Cyclic voltammetry was used to analyze the electrochemical properties of aGO-COL. The samples were dropped on a single carbon electrode (Zensor, SE100) and dried in an oven for one day, serving as a working electrode during the experiment. A silver wire was used as the auxiliary

electrode, and an Ag/AgCl electrode was used as the reference electrode. All electrodes were set together in a beaker containing 10 mM Fe(CN)₆³⁻ in 0.1 M phosphate-buffered saline (PBS) as the electrolyte. The voltage range was configured from –0.75 V to 1.25 V, and the scanning rate was 100 mV/s for five cycles. To measure the electrochemical reversibility and stability of aGO-COL, 100 scans were performed on the 64% aGO-COL samples with the same scan voltage and rate as described above.

2.4. Cell culture

PC-12 cells (rat adrenal pheochromocytoma cell line) were obtained from the Food Industry Research and Development Institute (BCRC 60048) in Taiwan and cultured in RPMI 1640 (Thermo Fisher, 11875093) with 5% fetal bovine serum (FBS, Corning, 35-076-EV) and 10% donor equine serum (HS, HyClone, SH30074). The cells were maintained in a humidified incubator at 37 °C and 5% CO₂, and the culture medium was exchanged every 2–3 days.

2.5. Cytotoxicity assays

To assess the biocompatibility of the aGO-COL composite, the cells were cultured on the aGO-COL-coated glass coverslip, and the cell viability and toxicity were tested. First, clean glass coverslips were treated with 0.1% poly L-lysine solution (Sigma-Aldrich, P4707) for 5 min, followed by a thorough wash with PBS and then treated with 32% and 64% aGO-COL and COL for 3 h. Subsequently, the PC-12 cells were seeded at 5 × 10⁴ cells/cm² on the aGO-COL and COL-coated substrates after the glass coverslips were rinsed three times with PBS and exposed to UV radiation for 15 min.

After culturing for 3 days, the cells were stained with calcein-AM and propidium iodide (PI) (BioScience, A017) to distinguish the proportion of live and dead cells by fluorescent imaging. The fluorescent images were taken with a confocal laser scanning microscope (Leica Microsystems, TCS-SP8) with excitation/emission wavelengths of 488/520 and 552/620 nm for calcein-AM and PI, respectively. In addition, cell viability was determined using a lactate dehydrogenase (LDH) assay kit (Dojindo, CK12). First, the lysis buffer was added to the wells of the positive control (100% cytotoxicity) and incubated at 37 °C for 30 min. Subsequently, the supernatant of each well of the samples was transferred into a 96-well plate, and then the working solution was added. After incubation at 37 °C for 30 min, the stop solution was added to each well, and the absorbance was measured at 490 nm using a microplate reader (Awareness Technology, ChroMate-4300). Finally, the cell viability was calculated by subtracting the average cytotoxicity.

2.6. Neuronal differentiation of the PC-12 cells

To induce differentiation of PC-12 cells on the aGO-COL-coated substrates, the culture medium was replaced with fresh RPMI 1640 medium supplemented with 50 ng/mL neuron growth factor (NGF, Thermo Fisher, 13257–019), 1% HS, and 1% penicillin-streptomycin after seeding the cells for 12 h. For differentiation experiments, the cells were seeded at a low density (1 × 10⁴ cells/cm²), and the differentiation medium was changed every 48–72 h. After 7 days of differentiation, the cells were stained with a fluorescence-conjugated anti-Tuj-1 (neuron-specific class III beta-tubulin) antibody. First, the cells were fixed with 4% formaldehyde solution for 15 min and blocked with PBS containing 5% FBS and 1% bovine serum albumin (BSA) for 1 h. After that, the cells were incubated with the antibody (BioLegend, A488-435L) for 1.5–2 h, and the nuclei were stained with Hoechst 33342 for 15 min. Finally, the cells were washed with PBS three times, and then the samples were sealed with mounting medium (Vector Laboratories, H-1000) to preserve fluorescence during long-term storage. The fluorescent images were captured with a confocal microscope, and morphological analysis of neurite coverage, length, and diameter was performed using ImageJ software and NeurphologyJ plugin [39].

2.7. Retinal prosthesis chip

The photovoltaic-powered 256-pixel subretinal prosthesis chip was fabricated using CMOS image sensor (CIS) technology. The retinal chip area was $3.2 \text{ mm} \times 3.2 \text{ mm}$, and each active pixel sensor (APS) area was $32.5 \mu\text{m} \times 85 \mu\text{m}$. The APSs were powered by on-chip photovoltaic cells to generate electrical stimulation [40]. A precision manual linear translation stage with a white LED was set up as a light irradiation device for an electrical test. An oscilloscope measured the stimulation current and clock frequency of a pixel to confirm different output voltages depending on the distance between the light source and the chip. The luminance of the LED at different distances from the retinal chip using a digital illuminance meter (TES electrical electronic, TES-1332 N).

For the cell culture experiment, the retinal chips were coated with COL and aGO-COL, as described previously. PC-12 cells (5×10^4 cells/cm²) were seeded on the chip and incubated for 12 h, after which the medium was replaced with the differentiation medium. Next, the cells were placed on the LED lamp irradiation platform for the subsequent electrical stimulation experiment, and the electrical stimulation signal was generated by the retinal chip and controlled by the LED switch. The Arduino UNO R3 microcontroller was used to program the LED switch to control the lights to be cyclically turned on for 1 min and off for 4 min for 1 h each day. After 5 days of electrical stimulation, the cells were stained with the *anti-Tuj-1* antibody (BioLegend, 801209) and observed under a confocal microscope as described above.

2.8. Preparation and characterization of micropatterns

A custom 3D bioprinter (developed by ARC Center of Excellence for Electromaterials Science, University of Wollongong, Australia) was used to print the micropatterned aGO-COL in a sterile laminar airflow cabinet. First, the aGO-COL composite was loaded into a syringe cartridge and a syringe barrel (Nordson, 7012074/3CC) with a 34G needle (Longze, 34G). The syringe was then connected to a dispensing controller (Iwashi, AD3000D) that accurately regulated nitrogen delivery, both in terms of pressure and output time. The micropattern array configuration and spacing were controlled using the MatterControl software (MatterHackers). After printing, the micropatterned aGO-COL was incubated at room temperature for 3 h and then washed twice with PBS. For the cell culture experiment, the cells were seeded at a density of 5×10^4 cells/cm² into a cell culture dish (TPP, 93040) with the aGO-COL micropatterns. After 24 h of culture, the cells were stained with Hoechst 33342 to visualize the specific attachment of the cells. The bright-field images of aGO-COL micropatterns were obtained with an upright light microscope (Leica Microsystems, DM2700 M), and fluorescence images of the cells were acquired using a confocal microscope.

2.9. Statistical analysis

GraphPad Prism 8.0 (GraphPad software) and OriginPro 9.1 (OriginLab Corporation) were used to analyze the data and plotted graphs. The data were expressed as the mean \pm the standard error of the mean. The statistical differences were analyzed using the one-way ANOVA test,

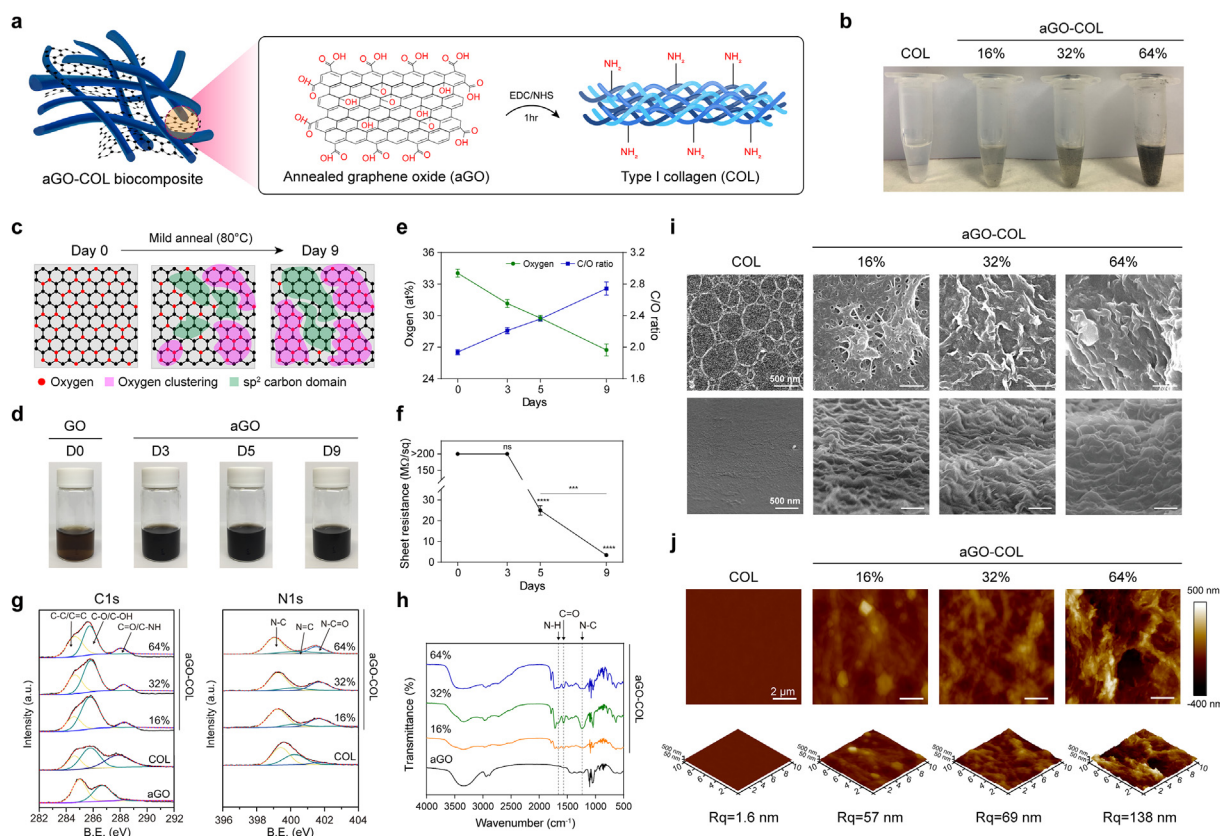


Fig. 2. Preparation and characterization of the aGO-COL composites. (a) Schematic and process diagram of the aGO-COL composites preparation. (b) Photographs of the aGO-COL at different weight percentages (16%, 32%, and 64%). (c) Schematic of the aGO surface characteristics with oxygen clusters and prominent graphitic structural (sp^2) domains. (d) Photographs of the aGO solution with different days of annealing treatment at 80°C . (e) Variation of oxygen content and C/O ratio of the aGO with different annealing days. (f) Comparison of the sheet resistance of the GO and aGO at different annealing days. (g) XPS spectra of C1s and N1s of the aGO, COL and aGO-COL composites. (h) FTIR spectra of the aGO, COL and aGO-COL composites. (i) Top view (above) and tilted view (below) SEM images of the COL and aGO-COL coated substrates. Scale bar, 500 nm. (j) AFM topography images of the COL and aGO-COL. Scale bar, 2 μm .

and P values less than 0.05 were considered statistically significant. *P < 0.05; **P < 0.01; ***P < 0.001; ns, non-significant.

3. Results and discussion

3.1. Preparation and characterization of the aGO-COL composites

Several studies have demonstrated that the COL matrix surface promotes neuronal cell differentiation [41]. Therefore, we conjugated the aGO with COL by covalent amide bonding to produce highly biocompatible and electroactive composites (0, 16, 32, and 64% w/w) (Fig. 2a and b).

The aGO was prepared according to a previous reported mild thermal annealing procedure that treated GO at 80 °C for 3, 5, and 9 days (aGO-D3, aGO-D5, aGO-D9) to enhance GO properties through temperature-driven oxygen diffusion and cluster formation [42]. This transforms the GO structure into prominent oxidized and graphitic domains (Fig. 2c). As shown in Fig. 2d, the color of the aGO suspension changed from yellowish-brown to black with increasing annealing time, indicating the presence of a clear aGO structure evolution. The C1s XPS spectra clearly show significant changes in the relative ratio of C=C (Fig. S1). Importantly, the structural evolution of aGO was gradually transformed from a mixed sp^2 - sp^3 hybridized carbon domain into sp^2 carbon domains, with no loss in the overall oxygen content (Fig. 2e). In addition, the measurement of the sheet resistance revealed that the increase in the sp^2 domains of aGO also enhanced the electron conduction efficiency. Compared to the GO electron conduction efficiency of $2 \times 10^8 \Omega/\text{sq}$ which exceeds the equipment limit, the efficiency of aGO-D5 and aGO-D9 decreased to $2 \times 10^7 \Omega/\text{sq}$ and $1 \times 10^6 \Omega/\text{sq}$, respectively (Fig. 2f). These results are consistent with previous reports at the same temperatures [42]. Notably, this structural evolution of aGO was attributed to both diffusion and transformation of oxygen atoms, which improved the electronic properties while maintaining a substantial number of oxygen functional groups. Subsequently, we chose aGO-D9 for the synthesis of the conductive aGO-COL composite because of its higher electrical conductivity.

To optimize the synthesis of the aGO-COL composites, we first attempted to determine the differences in crosslinking reactions at various molar ratios of 1-Ethyl-3-(3-dimethylaminopropyl) carbodiimide/N-hydroxysuccinimide (EDC/NHS) and pH values of 5.5–7.0. It was found that the aGO-COL composites were synthesized more efficiently by forming covalent bonds under the EDC/NHS ratio of 100:100 mM compared to 100:10 and 100:0 mM conditions (Fig. S2a). For the reactions at pH 5.5 and pH 7.0, there was no significant difference in the strength of the arylamine C–N bond (O=C–N) (Fig. S2b). Therefore, we adopted the 100:100 mM ratio of EDC/NHS and pH 5.5 as the optimal parameters for the chemical crosslinking reaction of the aGO-COL in this study. Collectively, the XPS full spectrum indicated that aGO-COL and COL have a specific additional N1s peak compared to aGO (Fig. S3). In addition, the C1s and N1s spectrums also revealed that the aGO-COL exhibited extra C=O/C–NH (288.2 eV) and N–C=O (288.2 eV and 401.7 eV) peaks compared to aGO (Fig. 2g). Fourier-transform infrared spectroscopy (FTIR) measurements also showed specific peaks of N–H (1560 – 1640 cm^{-1} and 3400 – 3500 cm^{-1}) and C–N (1100 – 1300 cm^{-1}) (Fig. 2h). These results clearly demonstrated the optimized crosslinking reaction of the aGO-COL composites and suggested the successful formation of a stable covalent reaction between aGO and COL through amide bonding. Incidentally, the aGO-COL-coated substrate presented a 3D crumpled surface morphology, whereas the COL-coated substrate had a 2D structure (Fig. 2i). The roughness of the wrinkles increased with the concentration of aGO, ranging from 57 nm for 16% aGO-COL to 138 nm for 64% aGO-COL (Fig. 2j). This 3D crumpled structure was perhaps formed by the aGO-COL crosslinking process in which aGO sheets were entrapped into fibrous collagen since a more significant sheet-like morphology was observed with increasing aGO concentration (Fig. S4). Notably, interfaces with crumpled and

roughened structures have been shown to enhance cell adhesion, proliferation, and differentiation [43,44].

We further investigated the electrochemical performance by cyclic voltammetry (CV) to study the effective electron transfer between the aGO-COL and the electrode surface (Fig. 3a and b). As shown in Fig. 3c, the oxidation wave of aGO-COL gradually shifted from +0.7 mV of the COL to +0.37 mV of the aGO (vs. Ag/AgCl), suggesting the presence of the aGO component in the aGO-COL composite. Compared to untreated GO, no oxidation or reduction waves were observed (Fig. S5). In addition, the peaks of the oxidation and reduction waves of aGO-COL increase with the percentage of aGO, indicating that the specific capacitance is dependent on the aGO concentration. The specific capacitance calculated from integration of the CV curves showed that the COL, 32% aGO-COL, and 64% aGO-COL were 0.43, 0.56, and 0.62 mF/g, respectively (Fig. 3d). In addition, we performed an electroactivity stability analysis for the 64% aGO-COL (Fig. 3e). After scanning the same sample 100 times, it was found that the oxidation and reduction peaks still existed, and no significant shifts were observed, suggesting that the aGO-COL has a stable electron flow and transfer reversibility under the circulating potentials.

Altogether, we successfully developed functional aGO-COL composites with self-assembled 3D crumpled structures. In particular, aGO prepared by the one-step mild thermal annealing procedure showed a 59% increase in electrical conductivity while maintaining the oxygen functional group, which can provide effective functional modifications. Additionally, we confirmed that aGO-COL improved the electrochemical properties of COL and exhibited stable electrical activity.

3.2. Growth and differentiation of PC-12 cells on the aGO-COL coated substrate

We then evaluated biocompatibility of the aGO-COL to determine whether it supports neuronal cell growth and differentiation. Therefore, a neuron-like PC12 cell line was cultured on the aGO-COL-coated substrates for subsequent analysis. Calcein-AM and propidium iodide (PI) solutions were used to visualize live and dead cells after 3 days of culture. As shown in Fig. 4a, there was no significant difference in the PI fluorescence signal emitted by the cells in the 32% aGO-COL and 64% aGO-COL compared to the COL sample. The cell compatibility of aGO-COL was further quantified by measuring the lactate dehydrogenase (LDH) release. High cell viabilities of 99% for change to the 32% aGO-COL and 94% for the 64% aGO-COL were recorded (Fig. 4b). These results indicated that the aGO-COL composite supported the growth of PC-12 cells and was not cytotoxic. Subsequently, we used nerve growth factor (NGF)-supplemented medium to induce PC-12 cell differentiation. After 7 days of differentiation, the cells were immunostained with *anti*-Tuj-1 antibody, which identifies neuron-specific class III beta-tubulin. From the confocal fluorescence images (Fig. 4c), it was observed that the 32% aGO-COL and 64% aGO-COL enhanced neuronal differentiation efficiency and increased neurite length (Fig. 4d and e). Notably, the neurites of PC-12 cells under the aGO-COL group were found to exhibit a microtubule bundle-like structure with an increase in the neurite diameter from 1.4 to 3.8 μm (Fig. 4f). Such microtubule bundles are crucial for neuronal function because extensive studies have shown that only bundles of neuronal cells are capable of axonal transport activity, while small caliber and ruptured neurites are not sufficient for reception and transmission of physiological signals [45]. One possible explanation for the aGO-COL-enhanced neuronal differentiation is attributed to its self-assembled 3D crumpled structure because cells noticeably attached centrally to the surface of the crumpled structure and were uniformly distributed to form small clusters on the aGO-COL-coated substrate (Fig. S6) [46]. Another possibility is that aGO exhibited superior performance in the adsorption of biomolecules. Our previous study [24] has demonstrated that the oxygen-containing functional groups and sp^2 domains in the aGO plane can enable efficient concentration of biomolecules in the aGO surface via van der Waals interactions and π - π

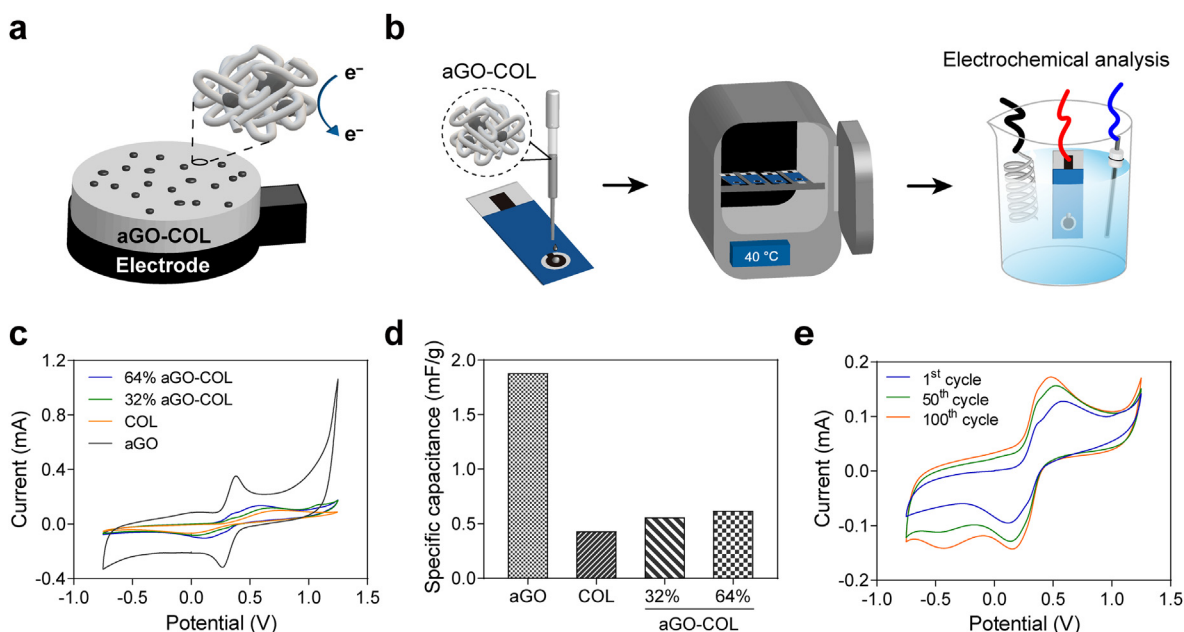


Fig. 3. Electrochemical properties of the aGO-COL composites. (a) Illustration of the electron transfer between the aGO-COL and electrode surface. (b) Schematic of the sample preparation steps for aGO-COL electrochemical analysis. (c) Cyclic voltammetry curves of the aGO, COL, 32% aGO-COL, and 64% aGO-COL. The scan rate was 100 mV/s. (d) The specific capacitance of aGO, COL, 32% aGO-COL, and 64% aGO-COL. (e) Cyclic performance of 64% aGO-COL at 1st cycle, 50th, and 100th cycle. The scan rate was 100 mV/s.

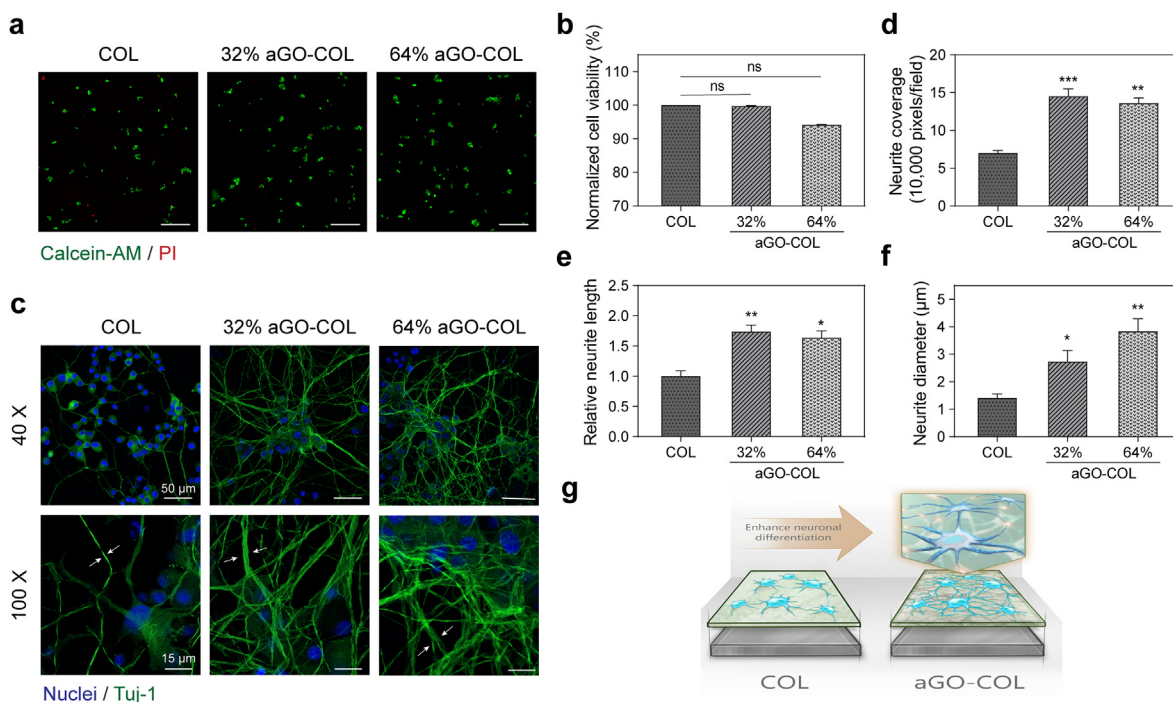


Fig. 4. Cytotoxicity and neural differentiation on the aGO-COL composites. (a) Fluorescence images of calcein-AM/PI stained PC-12 cells. The cells were cultured on COL, 32% aGO-COL, and 64% aGO-COL coated substrate for 3 days. Scale bar, 200 μm . (b) The LDH result of PC-12 cultured on COL, 32% aGO-COL, and 64% aGO-COL coated substrate. (c) Fluorescence images of Tuj-1 stained PC-12 cells after 7 days of differentiation on COL, 32% aGO-COL, and 64% aGO-COL coated substrate. Scale bar, 50 μm (40x magnification) and scale bar, 15 μm (100x magnification). (d–f) Quantification of neurite diameter, coverage and length of PC-12 cells cultured on the COL and aGO-COL interfaces. (g) Schematic of enhanced neurites differentiation of PC-12 cells on the aGO-COL coated substrate with crumpled interfaces.

stacking, thus enhancing cell differentiation. Importantly, recent studies have demonstrated that GO interfaces can mediate the transport of active substances to promote differentiation and axonal lengthening of neuronal cells [20,47]. These findings suggested that the aGO-COL with crumpled interfaces adequately supports PC-12 cell differentiation and

increases the neurite diameter over 2 times (Fig. 4g).

3.3. Coupling the neuronal cell with the retinal prosthesis chip

As a long-term implant in the retinal tissue, the adequate interaction

of the retinal prosthesis chip with optic nerve cells is critical in determining the efficiency of signal transmission [48]. Although functional surface modification of the chip electrodes with biomaterials can modify their surface properties, such as pulse transmission efficiency, electrochemical stability, and biocompatibility, it is relatively passive in terms of improving the inter-tissue interaction. A proactive strategy is to develop a biohybrid retinal chip that integrates biomaterials and living cells with synthetic electrodes [10], so that the retinal prosthesis chip not only has excellent electrode surface properties, but also has the potential to provide *in situ* tissue regeneration. Therefore, we attempted to culture the PC-12 cells on the aGO-COL-coated retinal chip, which is a photovoltaic self-powered implantable chip (Fig. 5a).

The retinal prosthesis chip was previously demonstrated to successfully activate retinal ganglion cells in adult rd1 mice [49], which integrates photodiodes, photovoltaic cells, charge pumps, and a microelectrode matrix (85 μm in length, 32.5 μm in width) (Fig. 5b). To use the photovoltaic self-powered chip to conduct cell culture experiments, we first designed a highly adjustable light-emitting diode (LED) lamp irradiation device (Fig. 5c, Fig. S7). The light irradiation device allowed the retinal chip to be arranged in the center of a 35 mm diameter culture dish and placed directly below the LED light source. The device

was also able to simultaneously perform three different experimental groups to activate the retinal chip, producing electrical stimulation. In addition, Fig. 5d shows that the intensity of the electrical stimulation generated by the microelectrodes depended on the distance between the LED and the retinal chip, which provided a voltage range of 40–100 mV. Previous studies have revealed that the differentiation efficiency and neurites growth of PC-12 cells were enhanced under an applied electric field intensity of 30–80 mV/mm [50]. Notably, the voltage excitation generated by the retinal chip was a biphasic square waveform of ~ 23.6 Hz rather than a unidirectional constant (Fig. 5e), which facilitated neurotransmitter communication between neurons more effectively [51]. After excluding the possibility of light or heat evoked cell differentiation by LEDs (Fig. S8), PC-12 cells were cultured for 5 days under electrical stimulation for 1 h per day to evaluate the growth and differentiation of neuronal cells on the retinal prosthesis chip. As shown in Fig. 5f, the neurites of PC-12 cells in the aGO-COL-coated retinal chip were observed to have a bundle-like structure with a thicker diameter than that of the COL-coated retinal chip. This result is consistent with the findings in the previous section, suggesting that the aGO-COL composite can stable modify the surface properties of a variety of material substrates, including glass (coverslips), plastic (cell culture vessels), and

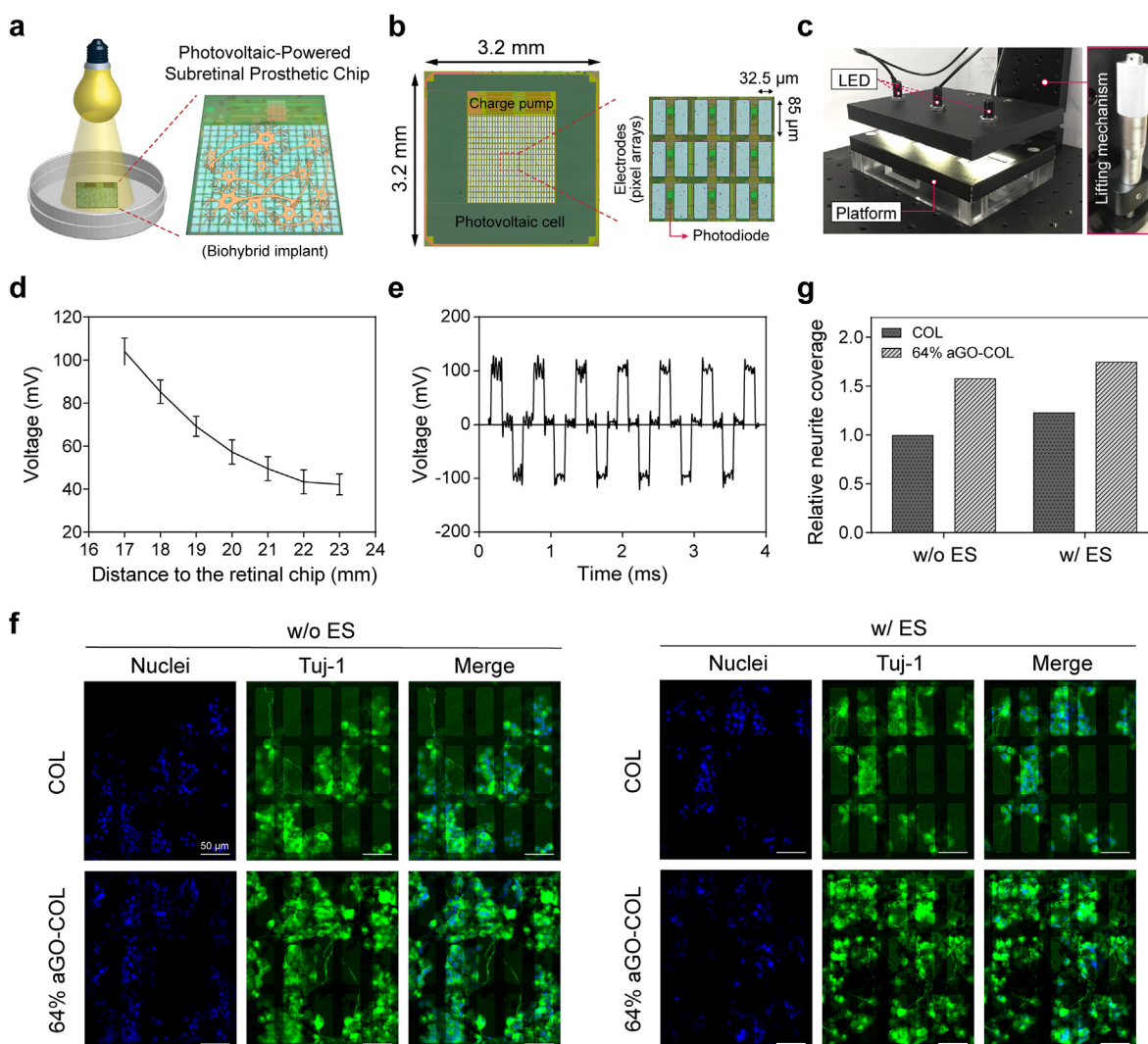


Fig. 5. Neuron differentiation on the retinal prosthesis chip. (a) Schematic of photovoltaic-powered retinal chip as a biohybrid neuron implant. (b) An optical image of the 3.2×3.2 mm retinal chip with 256 pixels and higher magnification shows the size of electrodes and photodiode position. (c) Photograph of a light irradiation device for electrical stimulation. (d) Variation of voltage intensity at different distances between the LED and the retinal chip. (e) The measured biphasic square voltage waveform on the retinal chip. (f) Fluorescence images of Tuj-1 stained PC-12 cells after 5 days of electrical stimulation on COL and 64% aGO-COL coated retinal chip. Scale bar, 50 μm . (g) Quantification of relative neurite coverage of PC-12 cells cultured on the retinal chip.

metallic aluminum (retinal prosthesis chips). Importantly, the aGO-COL-coated retinal chip showed more prominent differentiation trends under electrical stimulation (Fig. 5g) This was mainly attributed to the higher electrical conductivity provided by the aGO-COL-coated interface, supporting more efficient signal interaction and transmission between the external electric field injected by the electrodes and the neuronal cells. Collectively, the biohybrid retinal prosthesis chip with an aGO-COL-coated interface demonstrated enhanced neuronal differentiation and neurites growth under electrical stimulation.

As the performance of a retinal prosthesis ultimately depends on the electrode-neuron interface, the optimal situation would be expected to have a complete connection between the retinal prosthesis chip and the retinal tissue in the body. Thus, this strategy of creating a biohybrid electrode interface with the aGO-COL and neuronal cells offers the prospect of addressing the following limitations [11,13,16,17]: (1) foreign body reactions, (2) mechanical mismatch between tissues and implantable electrodes, and (3) signal transmission between the electronic and biological domains. Future development in biohybrid retinal prosthesis chips utilizing retinal neuronal cells derived from patient-derived induced pluripotent stem cells (iPSCs) would also be promising for autologous transplantation [52,53]. This may greatly increase the immunocompatibility of the retinal prosthesis chips while providing exciting opportunities to restore visual function through both tissue regeneration and electrical stimulation.

3.4. Developing the biohybrid retinal prosthesis with micropatterned aGO-COL

As the ultimate goal in biohybrid retinal prosthesis chip is to achieve micropatterns of functional biomaterials and living cells on the chip. This is because exposed surfaces other than electrodes in the actual

implantation must be covered and encapsulated with inert biocompatible materials to prevent unanticipated safety risks such as oxidative spalling of the retinal chip surface [54], blood clotting [55], and foreign body reactions [56]. In addition, the presence of a specific connection between the cells and electrodes also affects visual resolution reproduction [57, 58]. The single-point electrical signals generated by the retinal chip electrodes may experience crosstalk when the cells grow randomly and cover multiple electrodes in parallel. Therefore, experiments were conducted on the possibility of micropatterning aGO-COL to allow selective attachment of PC-12 cells.

A customized 3D bioprinter with droplet printing capability was utilized (Fig. 6a, Fig. S9). The printing parameters were optimized ($P = 1$ kPa, $F = 400$ mm/min) to print the smallest droplet size possible within the electrode ($85 \mu\text{m} \times 32.5 \mu\text{m}$) using a 34G needle ($80 \mu\text{m}$ inner diameter, $200 \mu\text{m}$ outer diameter). A contact-pin printing method was adopted to minimize droplet size and spread. As shown in Fig. 6b, the bright field image of the aGO-COL micropattern in the cell culture dish and the retinal chip was approximately $200\text{--}250 \mu\text{m}$. It was observed that each micropattern covered 4–6 microelectrodes, which is somewhat different from the size of the target electrodes. Although the micropattern size cannot be ideally matched to the electrode size, there is no doubt that the aGO-COL composite can still be adequately printed as uniform micropatterns. Importantly, when culturing the PC-12 cells on the aGO-COL micropatterned substrates, we observed that the cells were selectively attached to the aGO-COL micropattern (Fig. 6c). This result demonstrated that aGO-COL supported the formation of neuronal cell microarrays through an interface coating with specific micropatterns.

During the optimization process of the bioprinter, it was observed that the size of the micropatterns using the contact pin printing method depended on the outer diameter of the needle. Given that the needle size employed in this study was the smallest available size by the

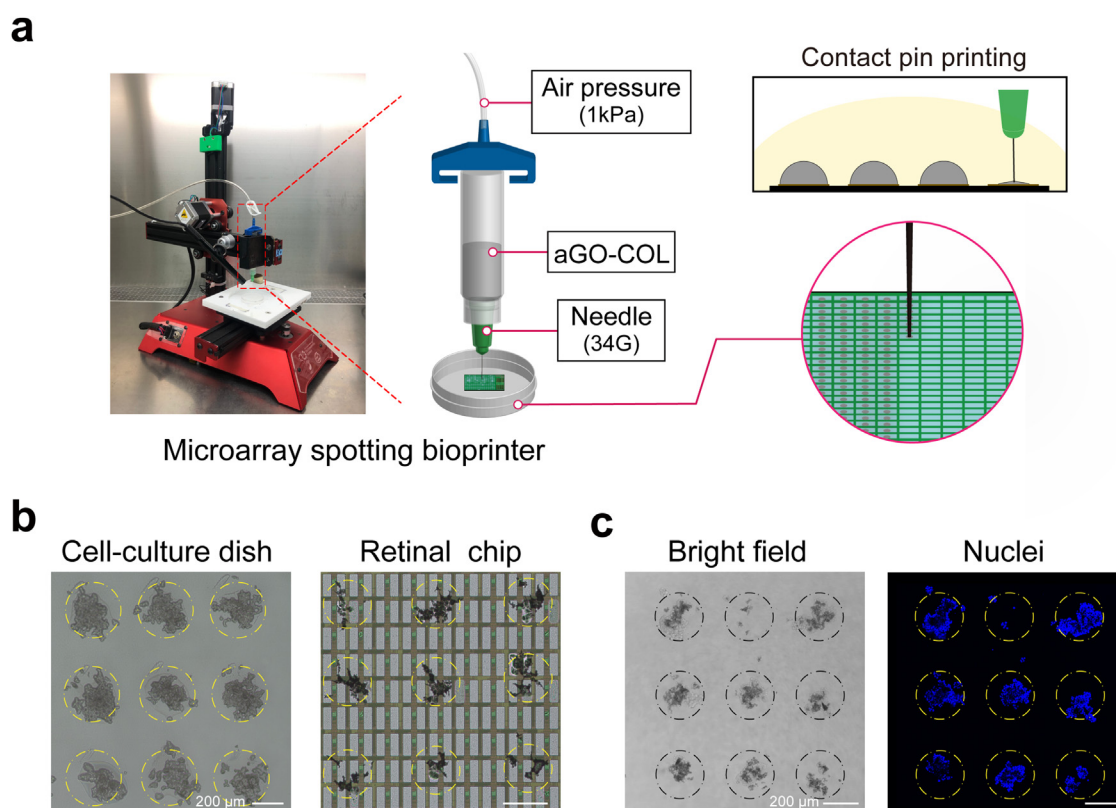


Fig. 6. Micropatterning of the aGO-COL composites. (a) Schematic of the aGO-COL micropatterning by the 3D bioprinter. The syringe loaded aGO-COL composite was patterned on the retinal chip through the contact pin printing method. (b) Bright-field images of aGO-COL micropatterns on the cell-culture dish (left) and the retinal chip (right). Scale bar, $200 \mu\text{m}$. (c) Bright-field image (left) and fluorescence images of nuclei staining (right) of PC-12 cell cultured on aGO-COL micropatterns. Scale bar, $200 \mu\text{m}$.

manufacturer, future studies can divert towards non-contact droplets printing methods such as piezoelectric inkjet printing or drop-impact printing systems, which could significantly reduce the minimum limit of micropattern size [59,60]. Several advanced bioprinting systems have recently demonstrated the possibility of producing cell micropatterns within 30 μm using drop-on-demand inkjet printing [61,62]. Notably, we also attempted to directly print cells by incorporating the PC-12 cells into the aGO-COL composite at a concentration of 1×10^7 cells/mL as a bioink (Fig. S10). The positive findings of successfully printing cell-encapsulated aGO-COL indicated that aGO-COL based bioink formulation can support neural cell printing. Overall, we demonstrated the possibility of creating specific neuronal cell-attached electrodes via the aGO-COL micropatterns. These results demonstrate that aGO-COL can support micropattern printing and serve as a bioink.

The micropatterned biohybrid electrode interface holds a niche that provides unique therapeutic opportunities and resources to restore and activate specific neurons in pathological tissues. For example, the transmission of visual messages in the optic nerve system is mainly summarized by the spatial receptive fields of retinal ganglion cells (RGCs) [63]. Therefore, electrical stimulation encoding specific signal pathways plays a critical role in reconstructing the bright spot size, color channels, and lightness contrast of the natural image in the light-evoked responses to maintain a high-resolution during processing [64]. In addition, the patterned biohybrid interface serves as a suitable bridge between biological and implantable electronic devices. It can also facilitate the design and fabrication of diverse electronic devices with good tissue compatibility.

4. Conclusions

In summary, we proposed a method to integrate PC-12 cells into a retinal prosthesis chip using an aGO-COL composite biomaterial and micropatterning printing technology. First, we confirmed that aGO increased the electrical conductivity by 59% compared to GO while retaining a large number of oxygen-containing functional groups to facilitate the cross-linking reactions of aGO-COL. Compared to natural COL, the aGO-COL not only exhibited better electrical activity, but also presented a unique self-assembled 3D crumpled surface structure on the substrate, which promoted neuronal cell differentiation and electrical stimulation efficiency of the retinal chip. Subsequently, we used droplet printing to create microscale patterns of the aGO-COL which successfully allowed the neuronal cells to selectively adhere to the micropatterned substrate, realizing the concept of biohybrid retinal prosthesis. The objectives of biohybrid implantable electrodes are different from those of other biocompatible implantable electrodes because the combination of autologous living cells will provide the advantage of low implant rejection and tissue regeneration [65,66]. These findings revealed an excellent opportunity to bridge the gap between biological and artificial implants for functional biohybrid retinal prostheses.

Credit author statement

J.-W.Y. and C.-Y.C. contributed equally to this work. J.-W.Y. and C.-Y.C.: Conceptualization, Methodology, Validation, Visualization, Investigation, and Writing - Original Draft. Z.-Y.Y.: Conceptualization, Methodology, and Investigation. J.H.Y.C. and X.L.: Resources and Writing - Review & Editing. C.-Y.W.: Resources, Project administration, Funding acquisition, and Writing - Review & Editing. G.-Y.C.: Conceptualization, Funding acquisition, Supervision and Writing - Review & Editing.

Data and materials availability

All data needed to support the conclusions are present in the paper and/or the Supplementary Materials. Additional data related to this paper may be requested from the authors.

Declaration of competing interest

The authors declare that they have no known competing financial interests or personal relationships that could have appeared to influence the work reported in this paper.

Acknowledgments

This work was supported in part by the Novel Bioengineering and Technological Approaches to Solve Two Major Health Problems in Taiwan, sponsored by the Taiwan Ministry of Science and Technology Academic Excellence Program, under Grant Number MOST 108-2633-B-009-001. G.-Y.C. would like to acknowledge funding from the Ministry of Science and Technology (MOST111-2636-E-A49-005-), Council of Agriculture, Executive Yuan (111AS-13.2.1-AD-U2) and the Higher Education Sprout Project of the National Yang Ming Chiao Tung University and Ministry of Education (111W20211), Taiwan. J.H.Y.C. and X.L. would like to acknowledge funding from the Australian National Fabrication Facility (ANFF) materials node and Australian Research Council Centre of Excellence Scheme (Project CE 140100012). The authors would like to thank Biomedical Electronics Translational Research Center (BETRC) at National Yang Ming Chiao Tung University in Taiwan for providing the photovoltaic self-powered retinal chip and assisting in retinal electrical stimulation signal measurement. The authors would also like to thank Dr. Cormac Fay from the University of Wollongong in Australia for building the customized 3D bioprinter.

Appendix A. Supplementary data

Supplementary data to this article can be found online at <https://doi.org/10.1016/j.mtbio.2022.100253>.

References

- [1] M.F. Dias, K. Joo, J.A. Kemp, S.L. Fialho, A. da Silva Cunha, S.J. Woo, Y.J. Kwon, Molecular genetics and emerging therapies for retinitis pigmentosa: basic research and clinical perspectives, *Prog. Retin. Eye Res.* 63 (2018) 107–131.
- [2] L.S. Lim, P. Mitchell, J.M. Seddon, F.G. Holz, T.Y. Wong, Age-related macular degeneration, *Lancet* 379 (9827) (2012) 1728–1738.
- [3] T.L. Edwards, C.L. Cottrill, K. Xue, M.P. Simunovic, J.D. Ramsden, E. Zrenner, R.E. MacLaren, Assessment of the electronic retinal implant alpha AMS in restoring vision to blind patients with end-stage retinitis pigmentosa, *Ophthalmology* 125 (3) (2018) 432–443.
- [4] L. da Cruz, J.D. Dorn, M.S. Humayun, G. Dagnelie, J. Handa, P.-O. Barale, J.-A. Sahel, P.E. Stanga, F. Hafezi, A.B. Safran, J. Salzmann, A. Santos, D. Birch, R. Spencer, A.V. Gideciyan, E. de Juan, J.L. Duncan, D. Elliott, A. Fawzi, L.C. Olmos de Koo, A.C. Ho, G. Brown, J. Haller, C.D. Regillo, L.V. Del Priore, A. Arditi, R.J. Greenberg, Five-year safety and performance results from the argus II retinal prosthesis system clinical trial, *Ophthalmology* 123 (10) (2016) 2248–2254.
- [5] A.C. Ho, M.S. Humayun, J.D. Dorn, L. da Cruz, G. Dagnelie, J. Handa, P.-O. Barale, J.-A. Sahel, P.E. Stanga, F. Hafezi, A.B. Safran, J. Salzmann, A. Santos, D. Birch, R. Spencer, A.V. Gideciyan, E. de Juan, J.L. Duncan, D. Elliott, A. Fawzi, L.C. Olmos de Koo, G.C. Brown, J.A. Haller, C.D. Regillo, L.V. Del Priore, A. Arditi, D.R. Geraschat, R.J. Greenberg, Long-term results from an epiretinal prosthesis to restore sight to the blind, *Ophthalmology* 122 (8) (2015) 1547–1554.
- [6] Y.H.-L. Luo, L. da Cruz, The Argus® II retinal prosthesis system, *Prog. Retin. Eye Res.* 50 (2016) 89–107.
- [7] J.D. Weiland, W. Liu, M.S. Humayun, Retinal prosthesis, *Annu. Rev. Biomed. Eng.* 7 (1) (2005) 361–401.
- [8] L.N. Ayton, N. Barnes, G. Dagnelie, T. Fujikado, G. Goetz, R. Hornig, B.W. Jones, M.M.K. Muqit, D.L. Rathbun, K. Stingl, J.D. Weiland, M.A. Petoe, An update on retinal prostheses, *Clin. Neurophysiol.* 131 (6) (2020) 1383–1398.
- [9] S. Picaud, J.-A. Sahel, Retinal prostheses: clinical results and future challenges, *Comptes Rendus Biol.* 337 (3) (2014) 214–222.
- [10] T. Yagi, Y. Ito, H. Kanda, S. Tanaka, M. Watanabe, Y. Uchikawa, Hybrid retinal implant: fusion of engineering and neuroscience, in: *IEEE SMC'99 Conference Proceedings. 1999 IEEE International Conference on Systems, Man, and Cybernetics* (Cat. No. 99CH37028), IEEE, 1999, pp. 382–385.
- [11] A.E. Rochford, A. Carnicer-Lombarte, V.F. Curto, G.G. Malliaras, D.G. Barone, When bio meets technology: biohybrid neural interfaces, *Adv. Mater.* 32 (15) (2020) 1903182.
- [12] T. Yagi, M. Watanabe, Y. Ohnishi, S. Okuma, T. Mukai, Biohybrid retinal implant: research and development update, in: *2005, Conference Proceedings. 2nd International IEEE EMBS Conference on Neural Engineering, 2005, IEEE, 2005, pp. 248–251.*

- [13] U.A. Aregueta-Robles, A.J. Woolley, L.A. Poole-Warren, N.H. Lovell, R.A. Green, Organic electrode coatings for next-generation neural interfaces, *Front. Neuroeng.* 7 (15) (2014).
- [14] Z. Aqrave, J. Montgomery, J. Travas-Sejdic, D. Svirskis, Conducting polymers for neuronal microelectrode array recording and stimulation, *Sens. Actuators B Chem.* 257 (2018) 753–765.
- [15] S.M. Won, E. Song, J. Zhao, J. Li, J. Rivnay, J.A. Rogers, Recent advances in materials, devices, and systems for neural interfaces, *Adv. Mater.* 30 (30) (2018) 1800534.
- [16] H. Yuk, B. Lu, X. Zhao, Hydrogel bioelectronics, *Chem. Soc. Rev.* 48 (6) (2019) 1642–1667.
- [17] R. Feiner, T. Dvir, Tissue–electronics interfaces: from implantable devices to engineered tissues, *Nat. Rev. Mater.* 3 (1) (2017) 17076.
- [18] N. Baig, M. Sajid, T.A. Saleh, Recent trends in nanomaterial-modified electrodes for electroanalytical applications, *Trac. Trends Anal. Chem.* 111 (2019) 47–61.
- [19] N. Jaiswal, I. Tiwari, Recent build outs in electroanalytical biosensors based on carbon-nanomaterial modified screen printed electrode platforms, *Anal. Methods* 9 (26) (2017) 3895–3907.
- [20] S. Shah, P.T. Yin, T.M. Uehara, S.-T.D. Chueng, L. Yang, K.-B. Lee, Guiding stem cell differentiation into oligodendrocytes using graphene-nanofiber hybrid scaffolds, *Adv. Mater.* 26 (22) (2014) 3673–3680.
- [21] D. Chen, H. Feng, J. Li, Graphene oxide: preparation, functionalization, and electrochemical applications, *Chem. Rev.* 112 (11) (2012) 6027–6053.
- [22] W. Yu, L. Sisi, Y. Haiyan, L. Jie, Progress in the functional modification of graphene/graphene oxide: a review, *RSC Adv.* 10 (26) (2020) 15328–15345.
- [23] Y. Wang, Z. Li, J. Wang, J. Li, Y. Lin, Graphene and graphene oxide: biofunctionalization and applications in biotechnology, *Trends Biotechnol.* 29 (5) (2011) 205–212.
- [24] J.-W. Yang, K.Y. Hsieh, P.V. Kumar, S.-J. Cheng, Y.-R. Lin, Y.-C. Shen, G.-Y. Chen, Enhanced osteogenic differentiation of stem cells on phase-engineered graphene oxide, *ACS Appl. Mater. Interfaces* 10 (15) (2018) 12497–12503.
- [25] J.-W. Yang, M.-L. Tseng, Y.-M. Fu, C.-H. Kang, Y.-T. Cheng, P.-H. Kuo, C.-K. Tzeng, S.-H. Chiou, C.-Y. Wu, G.-Y. Chen, Printable graphene oxide micropatterns for a bio-subretinal chip, *Adv. Healthcare Mater.* 7 (18) (2018) 1800365.
- [26] J.-W. Yang, Z.-Y. Yu, S.-J. Cheng, J.H.Y. Chung, X. Liu, C.-Y. Wu, S.-F. Lin, G.-Y. Chen, Graphene oxide-based nanomaterials: an insight into retinal prosthesis, *Int. J. Mol. Sci.* 21 (8) (2020) 2957.
- [27] D. Luo, G. Zhang, J. Liu, X. Sun, Evaluation criteria for reduced graphene oxide, *J. Phys. Chem. C* 115 (23) (2011) 11327–11335.
- [28] S. Pei, J. Zhao, J. Du, W. Ren, H.-M. Cheng, Direct reduction of graphene oxide films into highly conductive and flexible graphene films by hydrohalic acids, *Carbon* 48 (15) (2010) 4466–4474.
- [29] A.T. Smith, A.M. LaChance, S. Zeng, B. Liu, L. Sun, Synthesis, properties, and applications of graphene oxide/reduced graphene oxide and their nanocomposites, *Nano Mater. Sci.* 1 (1) (2019) 31–47.
- [30] L.J. Cote, J. Kim, Z. Zhang, C. Sun, J. Huang, Tunable assembly of graphene oxide surfactant sheets: wrinkles, overlaps and impacts on thin film properties, *Soft Matter* 6 (24) (2010) 6096–6101.
- [31] S. Deng, V. Berry, Wrinkled, rippled and crumpled graphene: an overview of formation mechanism, electronic properties, and applications, *Mater. Today* 19 (4) (2016) 197–212.
- [32] L.A. Tang, W.C. Lee, H. Shi, E.Y. Wong, A. Sadovoy, S. Gorelik, J. Holey, C.T. Lim, K.P. Loh, Highly wrinkled cross-linked graphene oxide membranes for biological and charge-storage applications, *Small* 8 (3) (2012) 423–431.
- [33] X. Shen, X. Lin, N. Yousefi, J. Jia, J.-K. Kim, Wrinkling in graphene sheets and graphene oxide papers, *Carbon* 66 (2014) 84–92.
- [34] P.V. Kumar, N.M. Bardhan, G.-Y. Chen, Z. Li, A.M. Belcher, J.C. Grossman, New insights into the thermal reduction of graphene oxide: impact of oxygen clustering, *Carbon* 100 (2016) 90–98.
- [35] N.M. Bardhan, P.V. Kumar, Z. Li, H.L. Ploegh, J.C. Grossman, A.M. Belcher, G.-Y. Chen, Enhanced cell capture on functionalized graphene oxide nanosheets through oxygen clustering, *ACS Nano* 11 (2) (2017) 1548–1558.
- [36] G.-Y. Chen, Z. Li, J.N. Duarte, A. Esteban, R.W. Cheloha, C.S. Theile, G.R. Fink, H.L. Ploegh, Rapid capture and labeling of cells on single domain antibodies-functionalized flow cell, *Biosens. Bioelectron.* 89 (Pt 2) (2017) 789–794.
- [37] S.R. Shin, C. Zihlmann, M. Akbari, P. Assawes, L. Cheung, K. Zhang, V. Manoharan, Y.S. Zhang, M. Yükksekaya, K.t. Wan, Reduced graphene oxide-gelMA hybrid hydrogels as scaffolds for cardiac tissue engineering, *Small* 12 (27) (2016) 3677–3689.
- [38] E. Yılmaz, B. Çakıroğlu, A. Gökçe, F. Fındık, H.O. Gulsoy, N. Gulsoy, Ö. Mutlu, M. Özacar, Novel hydroxyapatite/graphene oxide/collagen bioactive composite coating on Ti16Nb alloys by electrodeposition, *Mater. Sci. Eng. C* 101 (2019) 292–305.
- [39] S.-Y. Ho, C.-Y. Chao, H.-L. Huang, T.-W. Chiu, P. Charoenkwan, E. Hwang, NeuropHology: An automatic neuronal morphology quantification method and its application in pharmacological discovery, *BMC Bioinf.* 12 (1) (2011) 230.
- [40] C.-Y. Wu, C.-K. Tseng, J.-H. Liao, C.-C. Chiao, F.-L. Chu, Y.-C. Tsai, J. Ohta, T. Noda, CMOS 256-pixel/480-pixel photovoltaic-powered subretinal prosthetic chips with wide image dynamic range and Bi/Four-Directional sharing electrodes and their ex vivo experimental validations with mice, *IEEE Trans. Circ. Syst. I: Reg. Pap.* 67 (10) (2020) 3273–3283.
- [41] K. Brännvall, K. Bergman, U. Wallenquist, S. Svahn, T. Bowden, J. Hilborn, K. Forsberg-Nilsson, Enhanced neuronal differentiation in a three-dimensional collagen-hyaluronan matrix, *J. Neurosci. Res.* 85 (10) (2007) 2138–2146.
- [42] P.V. Kumar, N.M. Bardhan, S. Tongay, J. Wu, A.M. Belcher, J.C. Grossman, Scalable enhancement of graphene oxide properties by thermally driven phase transformation, *Nat. Chem.* 6 (2) (2014) 151–158.
- [43] J. Kim, J. Leem, H.N. Kim, P. Kang, J. Choi, M.F. Haque, D. Kang, S. Nam, Uniaxially crumpled graphene as a platform for guided myotube formation, *Microsyst. Nanoeng.* 5 (1) (2019) 1–10.
- [44] V. Rosa, H. Xie, N. Dubey, T.T. Madanagopal, S.S. Rajan, J.L.P. Morin, I. Islam, A.H.C. Neto, Graphene oxide-based substrate: physical and surface characterization, cytocompatibility and differentiation potential of dental pulp stem cells, *Dent. Mater.* 32 (8) (2016) 1019–1025.
- [45] E.M. Tanaka, M.W. Kirschner, Microtubule behavior in the growth cones of living neurons during axon elongation, *J. Cell Biol.* 115 (2) (1991) 345–363.
- [46] A.T. Nguyen, S.R. Sathe, E.K. Yim, From nano to micro: topographical scale and its impact on cell adhesion, morphology and contact guidance, *J. Phys. Condens. Matter* 28 (18) (2016) 183001.
- [47] D. Convertino, F. Fabbri, N. Mishra, M. Mainardi, V. Cappello, G. Testa, S. Capsoni, L. Albertazzi, S. Luin, L. Marchetti, C. Coletti, Graphene promotes axon elongation through local stall of nerve growth factor signaling endosomes, *Nano Lett.* 20 (5) (2020) 3633–3641.
- [48] A.Y. Chow, M.T. Pardue, V.Y. Chow, G.A. Peyman, C. Liang, J.I. Perlman, N.S. Peachey, Implantation of silicon chip microphotodiode arrays into the cat subretinal space, *IEEE Trans. Rehabil. Eng.* 9 (1) (2001) 86–95.
- [49] P.H. Kuo, O.Y. Wong, C.K. Tzeng, P.W. Wu, C.C. Chiao, P.H. Chen, P.C. Chen, Y.C. Tsai, F.L. Chu, J. Ohta, T. Tokuda, T. Noda, C.Y. Wu, Improved charge pump design and ex vivo experimental validation of CMOS 256-pixel photovoltaic-powered subretinal prosthetic chip, *IEEE (Inst. Electr. Electron. Eng.) Trans. Biomed. Eng.* 67 (5) (2020) 1490–1504.
- [50] W. Jing, Y. Zhang, Q. Cai, G. Chen, L. Wang, X. Yang, W. Zhong, Study of electrical stimulation with different electric-field intensities in the regulation of the differentiation of PC12 cells, *ACS Chem. Neurosci.* 10 (1) (2019) 348–357.
- [51] S. Ronchi, M. Fiscella, C. Marchetti, V. Viswam, J. Müller, U. Frey, A. Hierlemann, Single-cell electrical stimulation using CMOS-based high-density microelectrode arrays, *Front. Neurosci.* 13 (208) (2019).
- [52] Y. Wang, Z. Tang, P. Gu, Stem/progenitor cell-based transplantation for retinal degeneration: a review of clinical trials, *Cell Death Dis.* 11 (9) (2020) 793.
- [53] M. Mandai, A. Watanabe, Y. Kurimoto, Y. Hiram, C. Morinaga, T. Daimon, M. Fujihara, H. Akimaru, N. Sakai, Y. Shibata, M. Terada, Y. Nomiya, S. Tanishima, M. Nakamura, H. Kamao, S. Sugita, A. Onishi, T. Ito, K. Fujita, S. Kawamata, M.J. Go, C. Shinohara, K.-i. Hata, M. Sawada, M. Yamamoto, S. Ohta, Y. Ohara, K. Yoshida, J. Kuwahara, Y. Kitano, N. Amano, M. Umekage, F. Kitaoka, A. Tanaka, C. Okada, N. Takasu, S. Ogawa, S. Yamanaka, M. Takahashi, Autologous induced stem-cell-derived retinal cells for macular degeneration, *N. Engl. J. Med.* 376 (11) (2017) 1038–1046.
- [54] R. Daschner, U. Greppmaier, M. Kokelmann, S. Rudolf, R. Rudolf, S. Schleeauf, W.G. Wrobel, Laboratory and clinical reliability of conformally coated subretinal implants, *Biomed. Microdevices* 19 (1) (2017), 7–7.
- [55] A. Carnicer-Lombarte, S.-T. Chen, G.G. Malliaras, D.G. Barone, Foreign body reaction to implanted biomaterials and its impact in nerve neuroprosthetics, *Front. Bioeng. Biotechnol.* 9 (271) (2021).
- [56] J. Villalobos, D.A. Nayagam, P.J. Allen, P. McKelvie, C.D. Luu, L.N. Ayton, A.L. Freemantle, M. McPhedran, M. Basa, C.C. McGowan, A wide-field suprachoroidal retinal prosthesis is stable and well tolerated following chronic implantation, *Invest. Ophthalmol. Vis. Sci.* 54 (5) (2013) 3751–3762.
- [57] N.A.L. Chenais, M.J.I. Airaghi Leccardi, D. Ghezzi, Photovoltaic retinal prosthesis restores high-resolution responses to single-pixel stimulation in blind retinas, *Commun. Mater.* 2 (1) (2021) 28.
- [58] K. Mathieson, J. Loudin, G. Goetz, P. Huie, L. Wang, T.I. Kamins, L. Galambos, R. Smith, J.S. Harris, A. Sher, D. Palanker, Photovoltaic retinal prosthesis with high pixel density, *Nat. Photonics* 6 (6) (2012) 391–397.
- [59] C.D. Modak, A. Kumar, A. Tripathy, P. Sen, Drop impact printing, *Nat. Commun.* 11 (1) (2020) 4327.
- [60] R. Waasdorp, O. van den Heuvel, F. Versluis, B. Hajeer, M.K. Ghatkesar, Accessing individual 75-micron diameter nozzles of a desktop inkjet printer to dispense picoliter droplets on demand, *RSC Adv.* 8 (27) (2018) 14765–14774.
- [61] V. Ferrara, G. Zito, G. Arrabito, S. Cataldo, M. Scopelliti, C. Giordano, V. Vetri, B. Pignataro, Aqueous processed biopolymer interfaces for single-cell microarrays, *ACS Biomater. Sci. Eng.* 6 (5) (2020) 3174–3186.
- [62] Y.K. Kim, J.A. Park, W.H. Yoon, J. Kim, S. Jung, Drop-on-demand inkjet-based cell printing with 30-µm nozzle diameter for cell-level accuracy, *Biomicrofluidics* 10 (6) (2016), 064110-064110.
- [63] K.P. Johnson, L. Zhao, D. Kerschensteiner, A pixel-encoder retinal ganglion cell with spatially offset excitatory and inhibitory receptive fields, *Cell Rep.* 22 (6) (2018) 1462–1472.
- [64] S. Wienbar, G.W. Schwartz, The dynamic receptive fields of retinal ganglion cells, *Prog. Retin. Eye Res.* 67 (2018) 102–117.
- [65] L. da Cruz, K. Fynes, O. Georgiadis, J. Kerby, Y.H. Luo, A. Ahmado, A. Vernon, J.T. Daniels, B. Nommiste, S.M. Hasan, S.B. Gooljar, A.-J.F. Carr, A. Vugler, C.M. Ramsden, M. Bictash, M. Fenster, J. Steer, T. Harbinson, A. Willbrey, A. Tufail, G. Feng, M. Whitlock, A.G. Robson, G.E. Holder, M.S. Sagoo, P.T. Loudon, P. Whiting, P.J. Coffey, Phase 1 clinical study of an embryonic stem cell-derived retinal pigment epithelium patch in age-related macular degeneration, *Nat. Biotechnol.* 36 (4) (2018) 328–337.
- [66] Autologous induced stem-cell-derived retinal cells for macular degeneration, *N. Engl. J. Med.* 377 (8) (2017) 792–793.